

# Effect of an inverse parabolic confining electric potential on third harmonic generation in cylindrical quantum wires

TSHIPAMOletlanyi<sup>1</sup>

Department of Physics, University of Botswana, Gaborone, South east district, Botswana.

## ABSTRACT

A theoretical investigation of the effect of an inverse parabolic potential on third harmonic generation in cylindrical quantum wires is presented. The wave functions are obtained as solutions to Schrödinger equations solved within the effective mass approximation. It turns out that peaks of the third harmonic generation susceptibility (THGS) associated with nanowires of small radii occur at larger photon energies as compared to those associated with quantum wires of larger radii. The inverse parabolic potential red-shifts peaks of the THGS, and suppresses the amplitude of the THGS. THGS associated with higher radial quantum numbers is diminished in magnitude and blue-shifted, as a function of the photon energy. As a function of the inverse parabolic potential, the THGS is still characterized by peaks, which shift to lower values of the potential as the photon energy increases.

**Keywords:** Third harmonic generation; confining electric potential; cylindrical quantum wires.

## 1. Introduction

Advances in nanofabrication techniques have endowed the scientific community with an avenue of obtaining nanostructures of different sizes and geometries<sup>[1-3]</sup>. These nanostructures have applications in many disciplines like medicine<sup>[4,5]</sup>, chemical sensing<sup>[6]</sup>, optoelectronics<sup>[7, 8]</sup>, energy physics<sup>[9-11]</sup> and gas sensing<sup>[12]</sup>. An attractive feature of nanostructures is the emergence of quantization when charge carriers are confined to nanoscopic regions. The charge carriers occupy quantum states with associated energies, which are dramatically different from the bulk values. Electrons can make transitions between states if they absorb or lose energy which equals transition energies. This energy could be associated with photons, phonons or any other elementary excitation. Transition energies are the differences between energies of states between which transitions can take place, and can be modified by changing the size of the nanostructure or by changing the intrinsic electric potential of the nanostructure<sup>[13]</sup>. The ability of electrons to make transitions between different states renders nanostructures invaluable to nanodevice applications. Some of the interesting phenomena are non-linear optical processes. By making more than one transition to higher states, followed by a transition to a lower states, energy of radiation can be multiplied as required. *n*th harmonic generation is generation of electromagnetic wave with frequency *n* times the frequency of the input radiation. Examples are second harmonic generation (SHG), wherein the frequency of the incident radiation is doubled, third harmonic generation (THG), where the frequency is tripled, and so forth. However, THG has been shown to be more versatile than SHG in imaging samples<sup>[14]</sup>. It is thus instructive to study THG. Khodard theoretically studied third harmonic generation (THG) in a double ring shaped quantum dot and found that phonons have a significant effect on the third harmonic generation susceptibility (THGS)<sup>[15]</sup>. THGS can also be modified by the geometry of the nanostructure<sup>[16]</sup>. The effects of electric and magnetic fields on THGS in a Morse quantum well have also been investigated<sup>[17]</sup>. Bahari *et al* also looked at THG in multilayered nanoshells, and found that the THGS strongly depends on the thicknesses of the nanoshells<sup>[18]</sup>. THG has been experimentally achieved and studied<sup>[19]</sup>, and utilized, for example, to cool beryllium ions<sup>[20]</sup>.

In this communication, the effect of the inverse parabolic potential on the THGS of cylindrical quantum wires is investigated. The inverse parabolic potential is superimposed on an infinite cylindrical square well (ICSW). This paper

has the following organizational structure: Section 2 deals with the theoretical treatment of the problem, Section 3 relates the results and discussions, and the conclusions are laid in Section 4.

## 2. Theoretical Framework

The envisaged system is a free standing cylindrical quantum wire (CQW) of radius  $R$  and very long length hosting a negatively charged strand coincident with the axis of the wire, nonetheless considered to be much smaller than the radius of the nanowire. Through appropriate nanopatterning of the cylinder by varying the lattice composition, an intrinsic confining electric potential of the form

$$V(\rho) = \frac{1}{2} \mu \omega_0^2 R^2 \left( \frac{R^2}{\rho^2} - 1 \right) \quad (\rho < R) \quad (1)$$

and infinity elsewhere, may be realized. Here,  $\mu$  is the effective mass of the electron and  $\omega_0$  is the angular frequency associated with the classical harmonic oscillator. The Hamiltonian in cylindrical coordinates with this type of potential is separable, and the electron wave function can be cast in the form  $\psi(\rho, \phi, z) = C_{ml} F(\rho) \exp(ik_z z) \exp(im\phi)$ , where  $C_{ml}$  is the normalization constant,  $k_z$  is the axial wave number and  $m$  is the azimuthal quantum number that quantifies the quantized angular momentum of the electron. The radial portion of the electron wave function,  $F(\rho)$ , satisfies the second order differential equation (Schrödinger equation)

$$\frac{1}{\rho} \frac{d}{d\rho} \left( \rho \frac{dF(\rho)}{d\rho} \right) + \left\{ \frac{2\mu}{\hbar^2} [E_{ml} - V(\rho)] - \frac{m^2}{\rho^2} \right\} F(\rho) = 0. \quad (2)$$

where  $E_{ml}$  is the radial confinement energy. For the inverse parabolic potential (Eq. 1), the radial component of the Schrödinger equation is solvable in terms of the Bessel functions [13]

$$F(\rho) = C_1 J_\nu(\kappa\rho) + C_2 Y_\nu(\kappa\rho). \quad (3)$$

In the above,  $\kappa = \sqrt{\mu(2E_{ml} + \mu\omega_0^2 R^2)}/\hbar^2$  and  $\nu = \sqrt{m^2 + \mu^2 \omega_0^2 R^4}/\hbar^2$ . The nature of the Bessel Y function is such that it is divergent at the origin ( $\rho \rightarrow 0$ ), as such has to be discarded ( $C_2 = 0$ ) in the case of a solid cylinder, which leaves the radial wave function as

$$F(\rho) = J_\nu(\kappa\rho). \quad (4)$$

Imposing the condition that the electron wave function must vanish at the walls of the quantum wire due to the infinite potential outside the wire avails an expression for the determination of the energy eigen values for the electron as

$$E_{Tot} = E_{ml} + E_z = \frac{\hbar^2 j_{0ml}^2}{2\mu R^2} - \frac{1}{2} \mu \omega_0^2 R^2 + \frac{\hbar^2 k_z^2}{2\mu} \quad (5)$$

where  $j_{0ml}$  are the zeroes of the Bessel J function.

Third harmonic generation susceptibility

Consider the system under the influence of an electromagnetic field  $E(t) = \tilde{E} \exp(i\omega t) + \tilde{E} \exp(-i\omega t)$  incident along the  $z$  direction. We can invoke the time-dependent Liouville equation to investigate the evolution of the single electron state density matrix  $\hat{\rho}$

$$\frac{\partial \hat{\rho}_{ij}}{\partial t} = \frac{1}{i\hbar} [\hat{H}_0 - \hat{M}E(t), \hat{\rho}_{ij}] - \Gamma_{ij} (\hat{\rho} - \hat{\rho}^{(0)})_{ij}, \quad (6)$$

with  $\hat{H}_0$  being the unperturbed Hamiltonian of the system (with the electromagnetic radiation switched off),  $\hat{\rho}^{(0)}$  being the unperturbed density matrix and the perturbing term being  $-\hat{M}E(t) = -e\hat{r}E(t)$ , where  $e$  is the electronic charge and  $\Gamma_{ij}$  is the relaxation rate of  $\hat{\rho}$  to  $\hat{\rho}^{(0)}$ . Here,  $[\ ]$  denotes the quantum mechanical commutator. The above equation (Eq. (6)) can be solved using an iterative approach

$$\hat{\rho}(t) = \sum_n \hat{\rho}^{(n)}(t) \quad (7)$$

where

$$\frac{\partial \hat{\rho}_{ij}^{(n+1)}}{\partial t} = \frac{1}{i\hbar} \left[ \hat{H}_0, \hat{\rho}_{ij}^{(n+1)} \right]_{ij} - i\hbar \Gamma_{ij} \hat{\rho}_{ij}^{(n+1)} \left\} - \frac{1}{i\hbar} \left[ e\hat{r}, \hat{\rho}_{ij}^{(n)} \right] E(t). \quad (8)$$

The dependence of the electric polarization of the quantum wire on the electromagnetic field can be written as

$$P(t) = \left( \varepsilon_0 \chi^{(1)} \tilde{E} e^{i\omega t} + \varepsilon_0 \chi_0^{(2)} \tilde{E}^2 + \varepsilon_0 \chi_{2\omega}^{(2)} \tilde{E} e^{2i\omega t} + \varepsilon_0 \chi_{3\omega}^{(3)} \tilde{E}^3 e^{3i\omega t} \right) + c.c. \quad (9)$$

where  $\varepsilon_0$  is the absolute dielectric permittivity of classical vacuum while  $\chi^{(1)}$ ,  $\chi_0^{(2)}$ ,  $\chi_{2\omega}^{(2)}$  and  $\chi_{3\omega}^{(3)}$  are the linear, optical rectification, second harmonic generation and third harmonic generation susceptibilities, respectively [21]. c.c. is complex conjugate of the terms in the brackets. The THGS can be expressed as [15]

$$\chi_{3\omega}^{(3)} = \frac{e^4 \rho_e}{\varepsilon_0 \hbar^3} M_{01} M_{12} M_{23} M_{30} \times \left[ \begin{aligned} & \frac{1}{(\omega - \omega_{23} - i\Gamma_{23})(2\omega - \omega_{20} - i\Gamma_{20})(3\omega - \omega_{21} - i\Gamma_{21})} + \frac{1}{(\omega - \omega_{30} - i\Gamma_{30})(2\omega - \omega_{20} - i\Gamma_{20})(3\omega - \omega_{10} - i\Gamma_{10})} \\ & + \frac{1}{(\omega - \omega_{10} - i\Gamma_{10})(2\omega - \omega_{20} - i\Gamma_{20})(3\omega - \omega_{23} - i\Gamma_{23})} + \frac{1}{(\omega - \omega_{10} - i\Gamma_{10})(2\omega - \omega_{20} - i\Gamma_{20})(3\omega - \omega_{30} - i\Gamma_{30})} \\ & + \frac{1}{(\omega - \omega_{21} - i\Gamma_{21})(2\omega - \omega_{31} - i\Gamma_{31})(3\omega - \omega_{30} - i\Gamma_{30})} + \frac{1}{(\omega - \omega_{32} - i\Gamma_{32})(2\omega - \omega_{31} - i\Gamma_{31})(3\omega - \omega_{01} - i\Gamma_{01})} \\ & + \frac{1}{(\omega - \omega_{30} - i\Gamma_{30})(2\omega - \omega_{31} - i\Gamma_{31})(3\omega - \omega_{21} - i\Gamma_{21})} + \frac{1}{(\omega - \omega_{01} - i\Gamma_{01})(2\omega - \omega_{31} - i\Gamma_{31})(3\omega - \omega_{21} - i\Gamma_{21})} \end{aligned} \right], \quad (10)$$

where  $\rho_e$  is the electronic density,  $M_{ij} = \left\langle \psi_j | r | \psi_i \right\rangle$  the matrix elements of the dipole moment and  $\omega_{ij} = (E_j - E_i / \hbar)$  the transition frequency.

### 3. Results and Discussion

The parameters used in these calculations are  $0.067m_e$ , where  $m_e$  is the free electron mass, relevant to GaAS crystals. The other relevant parameters are:  $\rho_e = 10^{22} m^{-3}$  [22],  $\varepsilon_0 = 8.854 \times 10^{-12} F/m$ ,  $\hbar\Gamma_{10} = \hbar\Gamma_{21} = \hbar\Gamma_{32} = \hbar\Gamma_{30} = \hbar\Gamma$ ,  $\hbar\Gamma_{20} = \hbar\Gamma_{31} = \hbar\Gamma/2$  [15], where  $\hbar\Gamma = 2.156(meV)$  [18].

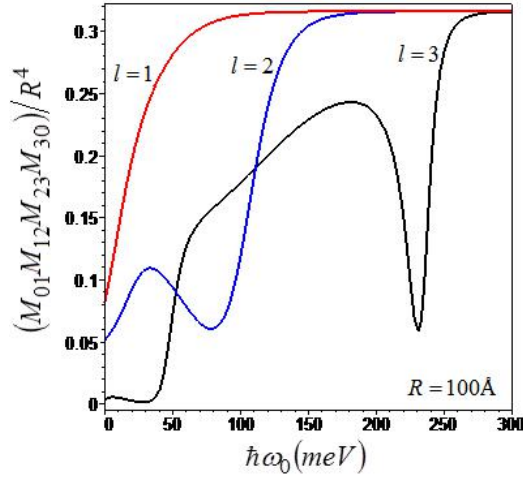


**Figure 1;** The dependence of the product of the matrix elements on the inverse parabolic potential for a quantum wire of radius of  $R = 100\text{\AA}$ , for the radial quantum numbers  $l = 1, 2$  and  $l = 3$

**Figure 1** illustrates the variation of the product of the matrix elements,  $M_{01}M_{12}M_{23}M_{30}$ , with strength of the inverse parabolic potential in a quantum wire of radius  $R = 100\text{\AA}$ . The three graphs have been generated for the radial quantum numbers  $l = 1, 2$  and  $l = 3$ , as indicated. The overall effect of the inverse parabolic potential is to increase the magnitude of  $M_{01}M_{12}M_{23}M_{30}$ . This is due to the fact that this potential tends to dilate the radial wave functions of electrons, which enhances the radial position vector. This effect is opposite to those of the magnetic field and the parabolic potential, which tend to suppress  $M_{01}M_{12}M_{23}M_{30}$  [22]. The variation of  $M_{01}M_{12}M_{23}M_{30}$  corresponding to higher radial quantum numbers is characterized by local minima and maxima, which are due to

the effect of the inverse parabolic potential on the electron wave functions [13].

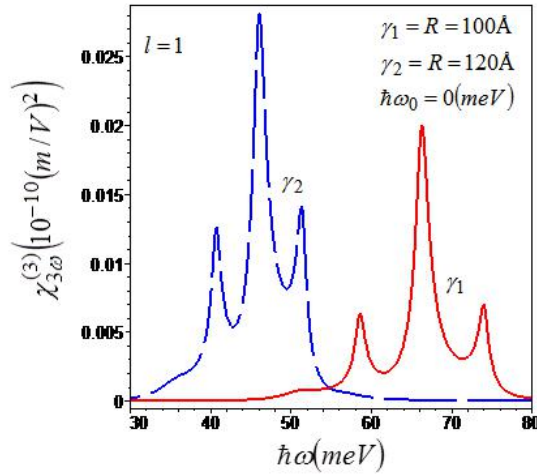


**Figure 2;** THGS as a function of the photon energy in an ICSW ( $\hbar\omega_0 = 0 (meV)$ ). The solid plot is for a quantum wire of radius  $R = 100\text{\AA}$  while the dashed curve is for  $R = 120\text{\AA}$

**Figure 2** depicts the ( $l = 1$ ) THGS as a function of the photon energy for a cylindrical nanowire without the intrinsic inverse parabolic potential ( $\hbar\omega_0 = 0 (meV)$ ). The solid plot corresponds to a cylindrical quantum wire of radius  $R = 100\text{\AA}$  while the dashed is associated with  $R = 120\text{\AA}$ . As can be appreciated from the figure, the peaks of the THGS become red-shifted as radius of the nanowire increases. This is due to the relaxation of the electron wave functions as the radius increases, which decreases radial confinement energy and consequently dwindles transition energies. The shifting of the peaks to lower photon energies is accompanied by increase in the magnitude of the THGS, which can be attributed to enhancement of the magnitude of the radial position vector as the radius increases. Additionally, the peaks of the THGS converge as the radius of the specimen is increased.

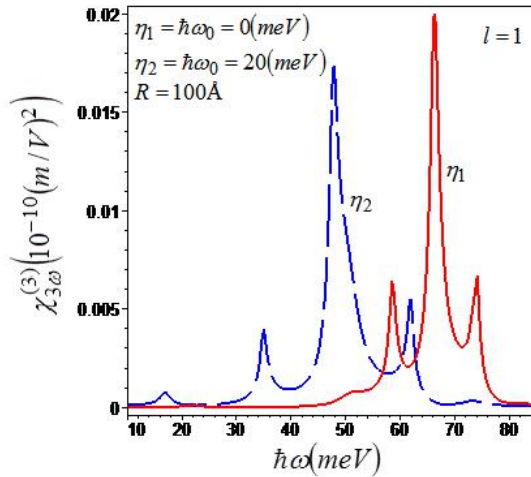


**Figure 3;** The variation of the THGS with the photon energy for a quantum wire of radius  $R = 100\text{\AA}$  without the inverse parabolic potential ( $\hbar\omega_0 = 0 (meV)$ ) (solid plot) and with the inverse parabolic potential of strength  $\hbar\omega_0 = 20 (meV)$  (dashed plot)

The effect of the inverse parabolic potential on the THGS can be viewed in figure 3, which depicts the THGS as a function of the photon energy for a cylindrical quantum wire of radius of  $R = 100\text{\AA}$ . The solid plot represents THGS of an infinite cylindrical square well (ICSW) ( $\hbar\omega_0 = 0 (meV)$ ) while the dashed curve is of a nanowire with an inverse parabolic potential of strength  $\hbar\omega_0 = 20 (meV)$  superimposed on the ICSW. The inverse parabolic potential affects the lower states than it does the higher, therefore it naturally decreases transition energies. This manifests as the red-shifting of peaks of the THGS. In addition, the inverse parabolic potential moves the peaks apart. This can be advantageous in cases where the peaks of the THGS need to be distinct from each other, for research and/or practical purposes. Another advantageous effect of the inverse parabolic potential is the enhancement of the THGS peaks at very low energies (in

this case, below the 40 meV region).

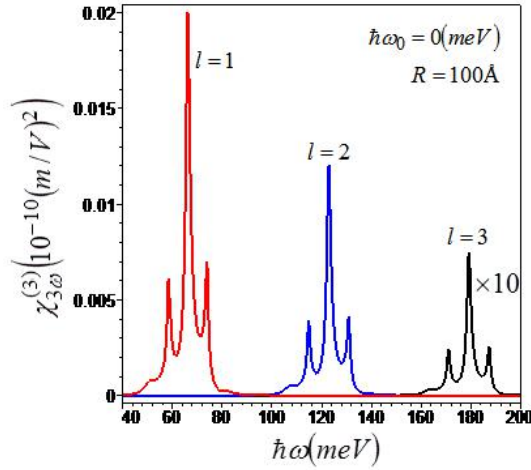


**Figure 4;** THGS as a function of energy of the radiation field for an ICSW ( $\hbar\omega_0 = 0(meV)$ ) of radius  $R = 100\text{\AA}$  corresponding to radial quantum numbers  $l = 1, 2$  and  $l = 3$

In figure 4, the THGS corresponding to an ICSW ( $\hbar\omega_0 = 0(meV)$ ) has been plotted as a function of the photon energy for the first three radial quantum numbers,  $l = 1, 2$  and  $l = 3$ . The radius of the nanowire is  $R = 100\text{\AA}$ . Transition energies associated with higher radial quantum numbers are greater than those associated with lower radial quantum numbers, hence the peaks of the THGS corresponding to higher radial quantum numbers occur at higher photon energies. Although not shown here for succinctness, the inverse parabolic potential will also red-shift the peaks of the THGS associated with higher radial quantum numbers. It can be seen from the figure that increasing the radial quantum number decreases the magnitude of the THGS, attributable to reduced overlapping of the radial electron wave functions which determine the THGS (Eq. 10).

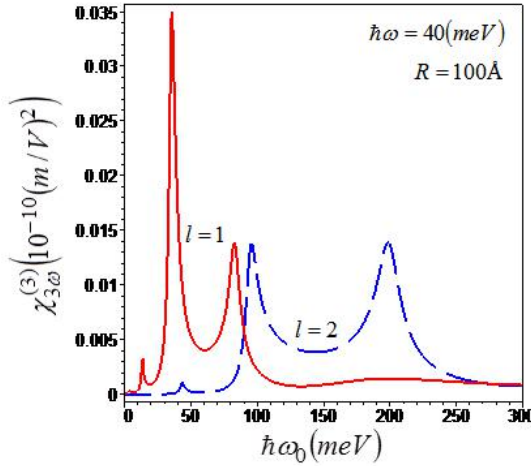


**Figure 5;** The dependence of the THGS on strength of the inverse parabolic potential in a quantum wire of radius  $R = 100\text{\AA}$ . The wire is irradiated with an electromagnetic field of energy  $\hbar\omega = 40(meV)$ . The solid plot is for radial quantum number  $l = 1$  while the dashed is for  $l = 2$

**Figure 5** illustrates the dependence of the THGS on strength of the inverse parabolic potential for fixed photon energy ( $\hbar\omega = 40(meV)$ ) in a cylindrical quantum wire of radius  $R = 100\text{\AA}$ . The solid curve represents the THGS corresponding to  $l = 1$  while the dashed curve is associated with  $l = 2$ . For a given photon energy, peaks of the THGS associated with greater radial quantum number occur at high values of the inverse parabolic potential. This is because, as already mentioned, transition energies associated with greater radial quantum numbers are usually higher than those of lower  $l$  values. Concomitantly, high values of  $\hbar\omega_0$  are required to reduce transition energies corresponding to large  $l$  to equal the photon energy.

## 4. Conclusion

The effect of the inverse parabolic potential on third harmonic generation in a cylindrical quantum wire has been investigated. The inverse parabolic potential is superimposed on an infinite cylindrical square well. The wave functions

were obtained by solving the Schrödinger equation within the effective mass approach. The third harmonic generation susceptibility corresponding to a quantum wire of larger radius is red-shifted and greater in magnitude than the THGS corresponding to a quantum wire of a smaller radius. The inverse parabolic potential red-shifts peaks of the THGS, and enhances peaks in the low energy region. The THGSs associated with greater radial quantum numbers have relatively small magnitude compared to those corresponding to lower values of the radial quantum number.

## References

1. Song C, Li X, Dong H, *et al.* Nondestructive tribochemistry-assisted nanofabrication on GaAs surface. *Sci. Rep.-UK* 2015; 5: 9020.
2. Santos A, Deen MJ, Marsal LF. Low-cost fabrication technologies for nanostructures: state-of-the-art and potential. *Nanotechnology* 2015; 26: 042001.
3. Li C, Zhao L, Mao Y, *et al.* Focused-ion-beam induced Rayleigh-plateau instability for diversiform suspended nanostructure fabrication. *Sci. Rep.-UK* 2015; 5: 8236.
4. Bwatanglang IB, Mohammad F, Yusof NA, *et al.* Folic acid targeted Mn:ZnS quantum dots for theranostic applications of cancer cell imaging and therapy. *International Journal of Nanomedicine-UK* 2016; 11: 413-428.
5. Wu J, Wang K, Peng Y. Advances in synthesis and application of nanometer drug carriers. *Characterization and Application of Nanomaterials* 2018; 1 (1): 12-18.
6. Ranjani M, Sathishkumar Y, Lee YS, *et al.* Ni-Co alloy nanostructures anchored on mesoporous silica nanoparticles for non-enzymatic glucose sensor application. *RSC Adv* 2015; 5: 57804-57814.
7. Chen J, Liu D, Al-Marri MJ, *et al.* Photo-stability of CsPbBr<sub>3</sub> perovskite quantum dots for optoelectronic application. *Sci. China Mater* 2016; 59(9):719-727.
8. Litvin AP, Martynenko IV, Purcell-Milton F, *et al.* Colloidal quantum dots for optoelectronics. *J. Mater. Chem. A* 2017; 5:13252-13275.
9. Lan X, Voznyy O, Kiani A, *et al.* Passivation using molecular halides increases quantum dot solar cell performance. *Adv. Mater* 2016; 28:299-304.
10. Xu W-P, Zhang Y-Y, Wang Q, *et al.* Thermoelectric effects in triple quantum dots coupled to a normal and a superconducting leads. *Phys. Lett. A* 2016; 380: 958-964.
11. Ding W-L, Peng X-L, Sun Z-Z, *et al.* Novel bifunctional aromatic linker utilized in CdSe quantum dots-sensitized solar cells: boosting the open circuit voltage and electron injection. *J. Mater. Chem. A* 2017; 5: 14319-14330.
12. Yang C, Xiao F, Wang J, *et al.* 3D flower- and 2D- sheet-like CuO nanostructures: Microwave assisted synthesis and application in gas sensors. *Sensor. Actuator. B-Chem* 2015; 207: 177-185.
13. Tshipa M. Oscillator strength for optical transitions in a cylindrical quantum wire with an inverse parabolic confining electric potential. *Indian J. Phys.* 2014; 88 (8): 849-853.
14. Weigelin B, Bakker G-J, Friedl P. Third harmonic generation microscopy of cells and tissue organization. *Journal of Cell Science* 2016; 129: 245-255.
15. Khordad R. Third-harmonic generation in a double ring-shaped quantum dot under electron-phonon interaction. *Opt. Commun.* 2017; 391: 121-127.
16. Li K, Guo K, Liang L. Effect of the shape of quantum dots on the third-harmonic generations. *Superlattice Microst.* 2017; 102: 300-306.
17. Restrepo RL, Kasapoglu E, Sakiroglu S, *et al.* Second and third harmonic generation associated to infrared transitions in a Morse quantum well under applied electric and magnetic fields. *Infrared Phys. Techn.* 2017; 85: 147-153.
18. Bahari A, Moghadam FR. Third order harmonics generation in multilayer nanoshells. *Opt. Commun.* 2012; 285: 3295-3299.
19. Fang X, Wei D, Wang Y, *et al.* Conical third-harmonic generation in a hexagonally poled LiTaO<sub>3</sub> crystal. *Appl. Phys. Lett.* 2017; 110: 111105.
20. Carollo RA, Lane DA, Kleiner EK, *et al.* Thrid-harmonic generation of a diode laser for quantum control of beryllium ions. *Optics Express* 2017; 25(7): 7220-7229.
21. Shao S, Guo K-X, Zhang Z-H, *et al.* Third-harmonic generation in cylindrical quantum dots in a static magnetic field. *Solid State Communications* 2011; 151: 289-292.
22. Wang G, Guo Q. Third-harmonic-generation in cylindrical parabolic wires with static magnetic fields. *Physica B* 2008; 403: 37-43.